Geophysical Journal International

Geophys. J. Int. (2022) **231,** 982–995 https://doi.org/10.1093/gji/ggac233
GJI Seismology

Upper crustal structure at the KTB drilling site from ambient noise tomography

Ehsan Qorbani [1], Petr Kolínský [2], Irene Bianchi,[3] Dimitri Zigone [4] and Götz Bokelmann [5]

[1] *International Data Center, CTBTO, 1400 Vienna, Austria. E-mail: ehsan.qorbani.chegeni@ctbto.org*
[2] *Institute of Geophysics, Czech Academy of Sciences, 117 20 Staré Město, Prague, Czech Republic*
[3] *Istituto Nazionale di Geofisica e Vulcanologia (INGV), 00143 Rome, Italy*
[4] *Institut Terre et Environnement de Strasbourg, Université de Strasbourg/CNRS, 67000 Strasbourg, France*
[5] *Department of Meteorology and Geophysics, University of Vienna, 1010 Vienna, Austria*

Accepted 2022 0. Received 2022 June 16; in original form 2021 October 15

SUMMARY

In this study, we show results from ambient noise tomography around the KTB (Kontinentales Tiefbohrprogramm der Bundesrepublik Deutschland), a continental deep drilling site located at the western edge of the Bohemian Massif, within the Variscan belt of Europe. At the KTB site, crustal rocks have been drilled down to 9 km depth. Before the drilling activity started, several active seismic surveys had been performed to explore its surroundings during the 1980s and early 1990s, in the frame of an extensive exploration of the area aimed at unravelling the characteristics of the continental lower crust that is exposed at surface in this location. Despite the exploration campaigns held at and around the KTB drilling site, there are important targets that are worth further investigation; these are related in particular to the obduction of lower crustal units to the surface, and to the mechanism of orogenic processes in general. Here we present a new 3-D shear wave velocity model of the area from cross-correlations of ambient seismic noise. The model is obtained by a unique data set composed of 2 yr of continuous data recorded at nine 3-component temporary stations (installed from July 2012 to July 2014) located on top and around the drilling site, and together with the data from 19 permanent stations throughout the region. This paper is focusing on the upper crustal layers, and we show velocity variations at short scales that correlate well with known geological structures in the region of the KTB site, at the surface and at depth. These are used to discuss features that are less well-resolved at present.

Key words: Seismic interferometry; Seismic noise; Seismic tomography; Crustal structure; Crustal imaging.

1 INTRODUCTION

The Variscan Belt is considered to be the suture zone between northern and southern Europe (Burrett 1972); the belt resulted from the continental collision between Laurussia and Gondwana, and a number of smaller plates in between, during Devonian and Carboniferous times. Our study area is located on top of the crystalline core region of the Variscan Belt, at the contact between the Saxothuringian and Moldanubian regions near the western edge of the Bohemian Massif. Reconstructing the palaeogeography and assessing a mutual correlation among outcropping units, has always been a hard task due to the fact that the tectonic units have been severely affected by high-grade metamorphism during the Variscan deformation (Franke 1989). The area has been intensively studied during the 1980s and 1990s, to find a suitable location for the KTB deep drilling site. The site has finally been chosen to shed light on the nature of the interactions between tectonic plates during the collision processes, by locating it in between the two major tectonic units (i.e. the Saxothuringian and the Moldanubian), and on top of a metamorphic body of lower-crustal origin (called ZEV, Zone of Erbendorf-Vohenstrauss). Despite the intensive programme of active seismic imaging campaigns (DEKORP research group 1988; Meissner & Bortfeld 1990) and the drilled borehole (Emmermann & Wohlenberg 1989; Emmermann & Lauterjung 1997, and references therein), there are open questions as to the nature of the contact between the two major units, the deep collision processes, and how the final obduction of the lower crustal units has occurred. KTB is an excellent region for unravelling these processes, that are central for reconstructing the evolution of the Variscan orogen itself, and also for understanding

the mechanisms of the orogenic processes in general (Enderle *et al.* 1998).

We aim to explore and infer new details on the crustal structures around the Variscan suture in central Europe, by performing ambient noise velocity tomography. Ambient seismic noise tomography is based on the reconstruction of virtual sources at every seismic station of an array by cross-correlating continuous seismic noise records between every pairs of stations (see Campillo & Roux 2015, for a review paper). Shapiro & Campillo (2004) demonstrated that dispersion characteristics of the virtual surface waves obtained from ambient noise correlations, are similar to those obtained from earthquakes, thus allowing the use of those virtual sources to perform traditional surface wave tomography methods (Shapiro *et al.* 2005). Since this technique does not rely anymore on any kind of active or passive punctual sources such as earthquakes, it can be used to image the structures of any kind of geological context with a resolution entirely governed by the geometry and density of the network (Shapiro *et al.* 2005; Zigone *et al.* 2015; Schippkus *et al.* 2019; Zigone *et al.* 2019; Qorbani *et al.* 2020). Using cross-correlation of ambient-noise data, we derived first a group-velocity map for Rayleigh wave. We then present a new local 3-D shear velocity model by applying two depth-inversion approaches. We discuss our new models for the upper 10 km structure with respect to the surface geology, tectonic features and previous seismic profiles at the KTB site.

2 GEOLOGICAL UNITS AND GEOPHYSICAL FEATURES OF THE CRUST

The study area is located in northeastern Bavaria which is geologically characterized by the presence of Variscan rocks, Mesozoic to Cenozoic sediments, and volcanics of Cenozoic age (Holzförster *et al.* 2011). The Variscan basement is subdivided into two main units, called Saxothuringian and Moldanubian. The Saxothuringian underwent post-variscan tectonics, is faulted by prominent NW–SE fault zones, among which the Franconian Lineament (FL), and has suffered low-medium pressure and high temperature metamorphism (Holzförster *et al.* 2011). The Moldanubian region includes large metamorphic areas intruded by granitic plutons during Variscan times. It is subdivided into the sensu stricto Moldanubian unit and the Zone of Erbendorf-Vohenstrauss (ZEV), where the KTB well has been drilled. The ZEV is composed by alternating paragneisses and amphibolites (Berckhemer *et al.* 1997); this unit is lithologically similar to the Münchberg Mass and to the Zone of Teplá-Barrandium; these three latter units together form the 'Bohemicum' unit (see map in Fig. 1). The FL fault system has been repeatedly activated under transpressive conditions, from Permo-Triassic till the Neogene; this led to 3000 m uplift of the KTB area (during Cretaceous to Palaeogene times), associated to hundreds of metres thick alluvial fan deposits that are still found at the western border of the lineament itself (Holzförster *et al.* 2011).

The area around the KTB site has been explored by geophysical investigations including a 3-D reflection survey (Dürbaum *et al.* 1990, 1992) and several 2-D wide-angle profiles which pointed out two main features: (1) a strong reflector in the upper crust of the KTB area that is steeply dipping towards the NE. It is attributed to the late and post-variscan FL and it has been verified by the presence of cataclastic rocks at about 7 km depth in the drilling site. And (2) a highly reflective area at the SE border of the drill site (Simon 1993). This is located in the middle crust (between 8 and 12 km depth) and bounded to the north and north-west by the Erbendorf Line (EL in Fig. 1); it displays high reflectivity and high seismic velocities. These geophysical properties (i.e. high velocity and high reflectivity) suggest an eclogitic to metabasic composition. Such middle crustal body has been called Erbendorf Body (EB) and is considered the unit from which the ZEV is derived. In the light of the previously listed observations, the ZEV has been interpreted not as a rootless nappe unit, but as an exhumed nappe, transported to the surface during a phase of transpressive deformation combined with further uplift and lateral displacements during the Variscan collision (Hirschmann 1996, and references therein).

3 DATA AND METHOD

3.1 Ambient noise data, pre-processing and computing cross-correlations

In this study, we used continuous recordings at 9 three-component broadband temporary stations installed from July 2012 to July 2014 located on top and around the KTB drilling site (Fig. 1, Bianchi *et al.* 2015). In order to improve the ray coverage and to extend the sampled area around the KTB site, we used continuous recordings over the same time period at 21 three-component permanent stations: 9 short period stations from Bayern Netz (BW), the network for monitoring local seismicity in the federal state of Bavaria, Germany (BW 2001); and 12 broad-band stations from Gräfenberg array (Harjes & Seidl 1977; Schweitzer *et al.* 2012) of the national seismological network (GR) in Germany (BGR 1976).

Before computing the cross-correlation functions, the continuous waveform data were preprocessed to increase the quality of the cross-correlations, and the resulting dispersion curves and the velocities. Here we have followed the preprocessing methodology applied in Zigone *et al.* (2015) and Qorbani *et al.* (2020). It consists of the following steps:

(1) Removing the instrument responses.
(2) High-pass filtering at 0.01 Hz.
(3) Glitch correction by clipping the data at 15 standard deviations.
(4) Removal of the transient signals (e.g. earthquakes) by cutting the daily records into 1 hr segments. We then perform an energy test. When the energy of a segment is greater than twice the standard deviation of the energy of the daily record, the 1 hr segment is removed.
(5) Whitening of the noise spectrum by dividing the amplitude by its absolute value between 1 and 100 s periods without changing the phase.
(6) Applying a second clipping by removing amplitudes larger than 3.5 standard deviations of the whitened records. This is done to reduce the influence of small seismic events that may have passed the energy test describe above.
(7) The data are downsampled to 10 Hz to reduce computational costs.

We reconstruct the Green's function of the medium between station pairs from cross-correlation of ambient noise simultaneously recorded at the two stations. Cross-correlations were computed for all station pairs, on daily records, and on all combinations of the three-components, vertical (Z), north–south (N) and east–west (E). The combinations result in nine intercomponents, ZE, ZN, ZZ, EE, EN, EZ, NE, NN and NZ. Distance between the station pairs is in a range of 3.3–135 km with an average of 53 km. We computed the cross-correlations for each day and for each intercomponent in the

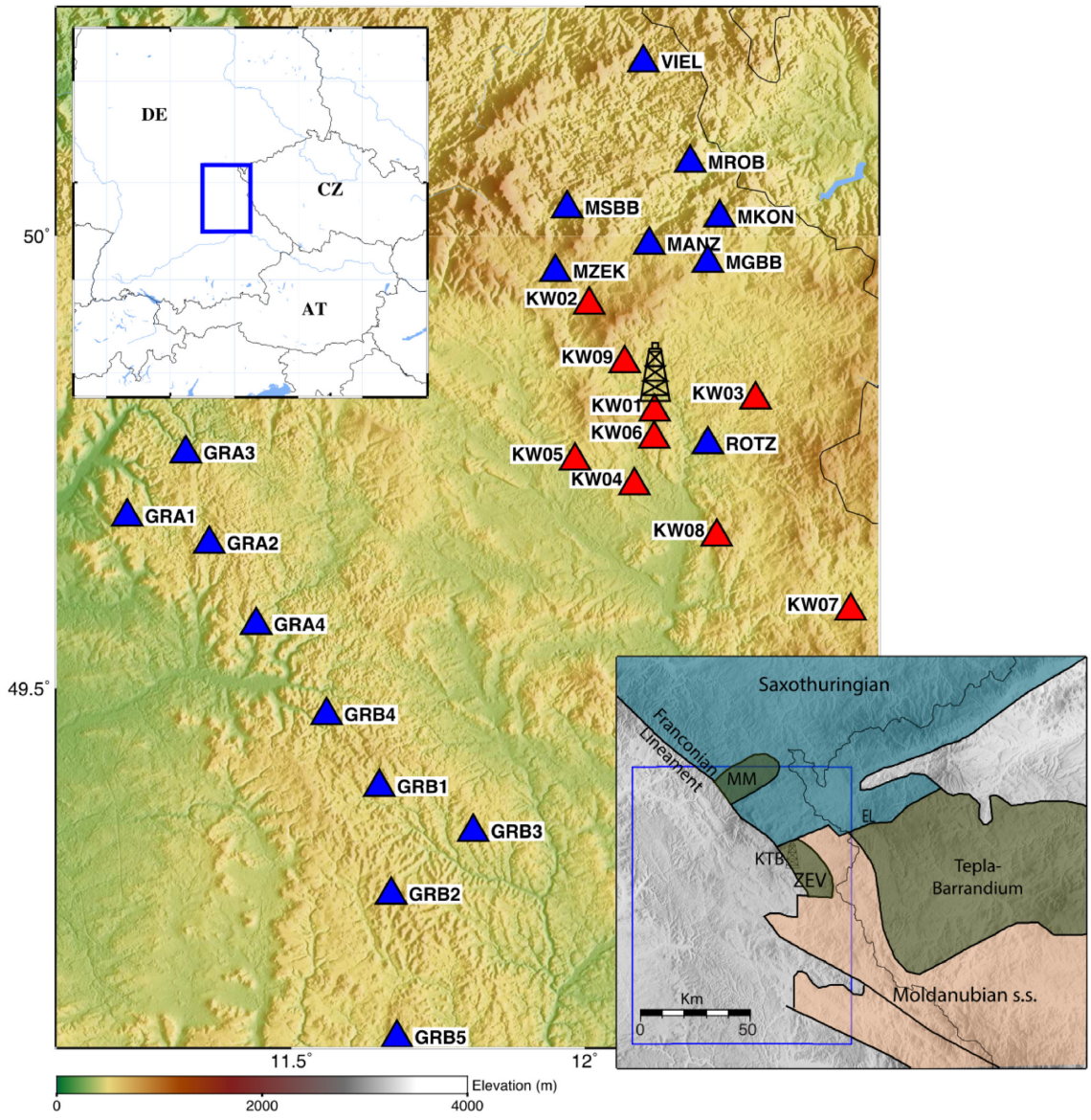

Figure 1. Study area with the location of seismic stations used in this work. Red for the stations belonging to the temporary KTB network (Bianchi *et al.* 2015). Blue for stations of the Bayern Netz (BW 2001) and German Regional Seismic networks (BGR 1976). Bottom right inset presents the greater study area showing the geotectonic units of the Bohemian Massif, based on Stettner (1992), and modified after Holzförster *et al.* (2011). ZEV, Zone of Erbendorf-Vohenstrauss; MM, Münchberg Masse; EL, Erbendorf Line. The blue rectangles show the study area of this work.

frequency domain. The computed daily correlation function is the average of the 1 hour segments which are left after the preprocessing steps mentioned before. The cross-correlations are two-sided time functions, called causal and anticausal with positive and negative correlation lags, respectively. In order to minimize the seasonal effect of the noise source we returned the cross-correlations to the time domain to be able to stack them over the 2 yr of data. The stacked cross-correlations were then rotated according to the interstation azimuth to obtain the correlations on the radial (R), transverse (T) and vertical (Z) components.

We used ambient noise in the microseism band that is dominated by surface waves (e.g. Toksöz & Lacoss 1968; Campillo & Roux 2015). Because of the overall lower quality data on the horizontal components, especially for temporary stations, we focused our efforts on obtaining reliable Rayleigh waves by combining the information on the RR, RZ, ZR and ZZ components. Example of the cross-correlations on three station-pairs, KW02-KW07, KW04-MANZ and GRB3-VIEL on the four intercomponents (ZZ, RR, RZ and ZR) containing the Rayleigh wave are shown in Fig. 2. Fig. S1 shows the correlation tensor, which represents propagation of surface waves through all station pairs. We selected the cross-correlations that have signal-to-noise ratio (SNR) larger than 5. The SNR is defined here as max amplitude of the cross-correlation divided by the standard deviation of a noise window. Accordingly, out of total 435 computed cross-correlations from initially 30 stations, we selected 378 cross-correlations from 28 stations (shown in Fig. 1).

3.2 Measuring velocity dispersion

Group-velocity dispersion curves were measured on merged causal and anticausal parts of the cross-correlations for the four

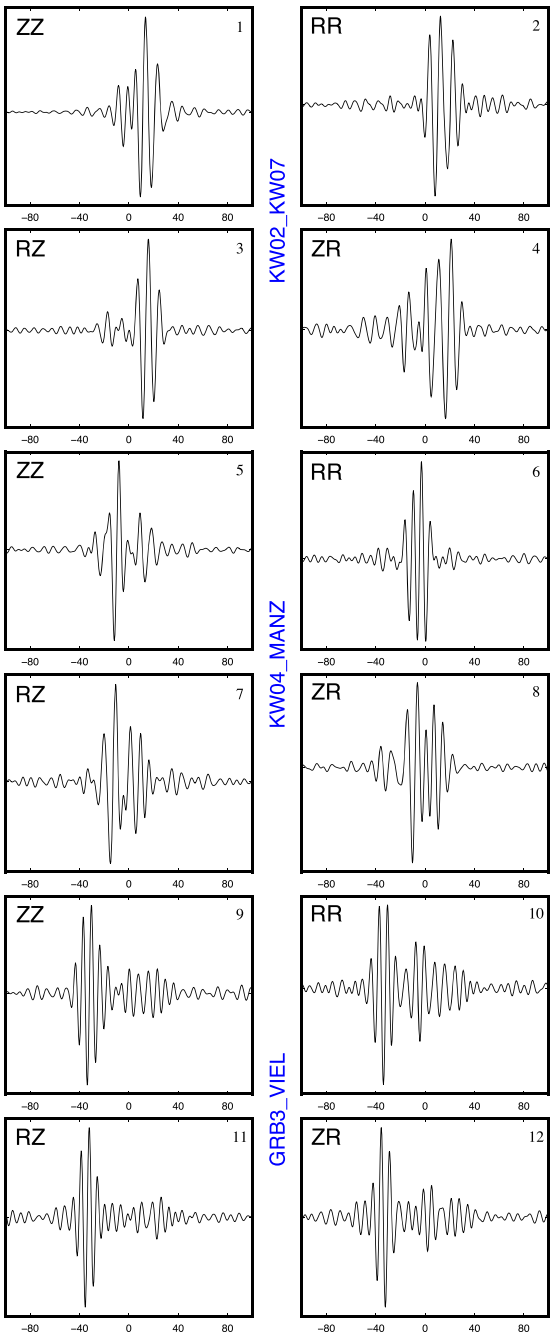

Figure 2. Examples of cross-correlations on the ZZ, RR, RZ and ZR intercomponents. The cross-correlations are stacked over the 2 yr of data and rotated. Top four panels (1–4) show cross-correlations between stations KW02 and KW07, four middle panels (5–8) show the same for the stations KW04 and MANZ, and four lower panels (9–12) for the stations GRB3 and VIEL.

intercomponents of the correlation tensor, RR, ZZ, RZ and ZR, which contain Rayleigh waves. We used the method developed in Kolínský & Brokešová (2007). It uses multiple-filtering in the frequency domain with around 140 Gaussian filters in the period range of 0.3–8.0 s. The filters have non-constant relative resolution with filter width linearly depending on period. Towards longer periods, the filters span broader range of periods. Filtered spectra are transformed back to the time domain. Hence we obtain a set of quasiharmonic signals, for which we calculate their envelopes. We first pick all local maxima of all the envelopes for the given cross-correlation component. The group-velocity dispersion curve estimation then starts from the longest wave, where the fundamental mode is clearly identified and continues to shorter period waves, selecting always the dispersion branch which is the closest to the point in time of the previous envelope regardless of its amplitude. This allows to pick the fundamental mode even for shorter periods, where other wave groups have larger amplitudes. Therefore, the dispersion curves do not suffer by mistakenly picked higher modes or body-wave arrivals. Tests of the method can be found in Kolínský *et al.* (2011). The method was recently used in Lukešová *et al.* (2019). Fig. 3 shows period-group velocity diagrams for three profiles of different lengths (and different tectonic units). We see a complex distribution of energy in the velocity-period plane with smooth group-velocity dispersion curves picked.

We tested several width settings of the filters and we used the one, for which a small change of the filter widths did not cause any change of the group velocity. The dispersion curve can then be considered as filter-independent. The processing was done in an automatic fashion. In total, we processed 378 cross-correlations. We obtained four independently determined dispersion curves from each cross-correlation (on RR, RZ, ZR and ZZ intercomponent). We identified 90 cross-correlations (around one quarter of all), which yielded different curves for each of the four components and hence needed to be processed manually. During the manual processing, all four components were taken into account to set the filter widths so that a similar group-velocity dispersion curve was determined at all four of them.

Afterward, in order to ensure good quality of dispersion curves, we extracted the Rayleigh-wave dispersions by stacking the RR, RZ, ZR and ZZ. For each station pair and at each period, we selected velocities from each of the ZZ, RZ, ZR and RR if they were within ±10% of the mean velocity at that period. The dispersion curves that passed these criteria, were used for group velocity inversion. The entire set of group velocities is shown in Fig. S2.

4 GROUP-VELOCITY TOMOGRAPHY

4.1 Velocity inversion

To obtain tomographic images of the Rayleigh-wave group velocity, the dispersion data were inverted using the method of Barmin *et al.* (2001). The forward problem is given as $d = Gm$, where $d = t_{\mathrm{obs}} - t_{\mathrm{mod}}$, defined as the difference between observed and modeled traveltime. The matrix G consists of travel times in each cell of the initial model for each path. The group velocity model is $m = (u - u_0)/u_0$ where u_0 is the initial velocity and u is the velocity after the inversion. The Barmin method is a damped least-square inversion, which is based on minimizing the penalty function shown below. It comprises a linear combination of data misfit, model smoothness, and magnitude of perturbations.

$$(G(m) - d)^T (G(m) - d) + \alpha^2 \|F(m))\|^2 + \beta^2 \|H(m)\|^2 .$$

The model smoothness is controlled by a Gaussian spatial smoothing function F over 2-D grids, with a correlation length (σ) and a damping factor (α).

$$F(m) = m(r) - \int_s exp\left(-\frac{|r - r'|^2}{2\sigma^2}\right) m(r')\mathrm{d}r'.$$

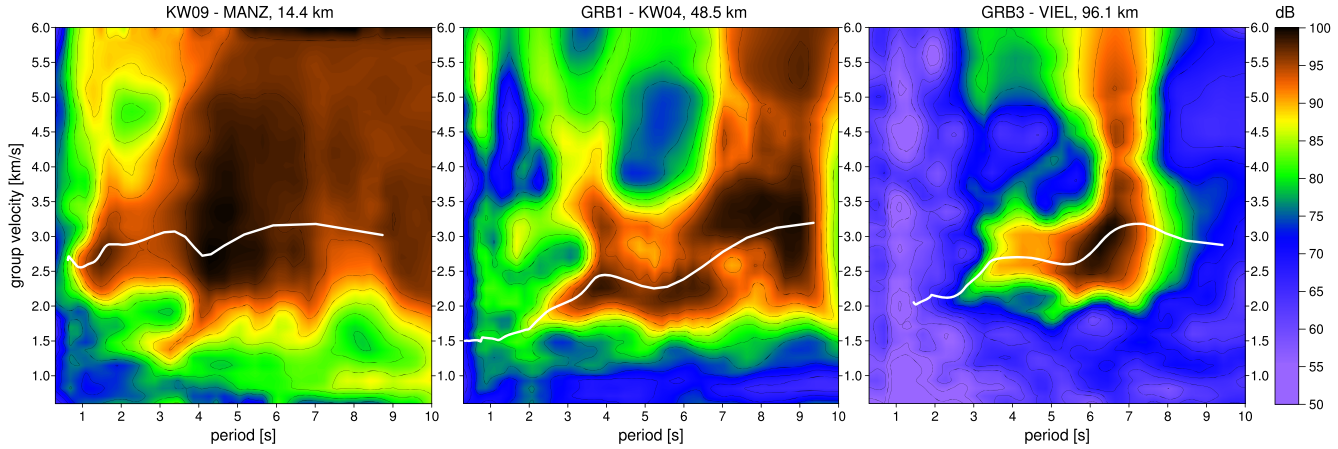

Figure 3. Examples of group-velocity dispersion curves measured on ZZ intercomponents, overlaid on top of the spectrograms. Left-hand panel shows the curve measured over a shorter interstation path through the Variscan basement. Middel panel shows the curve measured over medium-length interstation path through the Mesozoic Basin units, and right-hand panel shows the curve over a long path crossing the whole region.

The function H is defined as $H(m) = \exp(-\lambda\rho)m$, where λ is a weight factor that produces a gradual fading of the inverted model into the initial model in cells where the path density is low. ρ defines the path density. The two parameters, λ and β, control the magnitude of the model perturbation. When the ray coverage is relatively good, these two parameters have little effect on the final model (e.g. Stehly *et al.* 2009; Poli *et al.* 2013; Zigone *et al.* 2015). We thus fix the λ and β at 0.4 and 3, respectively. We used a grid size of 2 km and tested a range of values for the correlation length (σ) and damping factor (α). These two parameters control the spatial smoothing. Having done an L-curve analysis (e.g. Hansen & O'Leary 1993; Stehly *et al.* 2009), the optimized values for σ and α were selected according to the variation of the variance reduction of the models with respect to parameters (σ, α) at each period range (see Qorbani *et al.* 2020, for more detail). We then performed the inversion for group velocity using an initial model which is the average group velocity at each period. The obtained group-velocity map of Rayleigh waves is presented in Fig. 4 at 0.4, 2, 4 and 8 s of period. The high and low-velocity anomalies on both side of the Franconian Lineament (FL) match very well with the Variscan basement to the NE of the FL and the Mesozoic Basin units to the SW respectively. We will discuss more the retrieved features on the shear wave velocity model in Section 6.

4.2 Tomography resolution

We assessed the resolution of the group-velocity tomography from the path density and also directly from the resolution matrix as it has been suggested to be a more robust way of quantifying tomography resolution (Lévêque *et al.* 1993; Barmin *et al.* 2001). Path density maps at 3, 5 and 9 s of period are presented in Fig. 5. For most of the cells in the region, the path coverage is acceptable with 6 paths per cell on average at 9 s period and up to 10 paths per cell on average at the shorter periods, 3 and 5 s. Using the resolution matrix of the inversion we also evaluated the resolution by quantifying the dependence of the modelled group velocity at each cell on the other cells. This quantification provides a correlation length—defined as the distance at which the value of the resolution matrix is reduced to half—which is an estimation of the averaging width (in km) for each cell of the model (Barmin *et al.* 2001)—thus an estimation of spatial resolution of the model.

The spatial projection of the resolution matrices for each cell is not symmetric, hence, there are a worst and a best direction for the correlation length reflecting the non-circular shape of the averaging process. We present in Fig. 5 the correlation length in both the worst and the best directions as well as the mean correlation length for each cell at a 5 s centre period. As shown in Fig. 5(f), the averaging width is about 2–9 km in the best direction for most of the study region. It however, increases to about 15 km at the southeastern edge of the region. The mean correlation length is 5–7 km in the study region (Fig. 5e), which seems sufficient to resolve the geological features in the targeted area.

5 SHEAR WAVE VELOCITY INVERSIONS

To obtain 3-D shear velocity (v_S) model of the region, we applied two approaches in order to improve the reliability of the velocity model. They are described in the following sections. As input to both approaches, the local group-velocity dispersion curves were constructed from the group-velocity maps at each cell (2×2 km) of the grid.

5.1 Depth inversion—approach 1

In the first approach, we used the linearized inversion procedure of Herrmann (2013), through which the local dispersion curves are inverted to obtain a local 1-D shear-velocity model at each cell. These 1-D models are combined to obtain a 3-D shear-velocity model for the region. Due to the linearized scheme of the inversion, the accuracy of the final model strongly depends on the initial velocity model. Therefore, to construct a good and reliable initial model, we first extracted an average dispersion curve from all the cells. The average dispersion curves were then inverted to achieve an average 1-D model using an 1-D starting model (Bianchi & Bokelmann 2018), which was derived by receiver functions at the same temporary stations used in this study. We used this resulting average v_S model as initial model for inverting the local dispersion curves in each cell of the grid. We included the group velocities of periods between 0.3 and 13 s.

The inversion was set to 32 layers of constant thickness, 0.5 km, above a half-space. During the inversion, shear velocities could

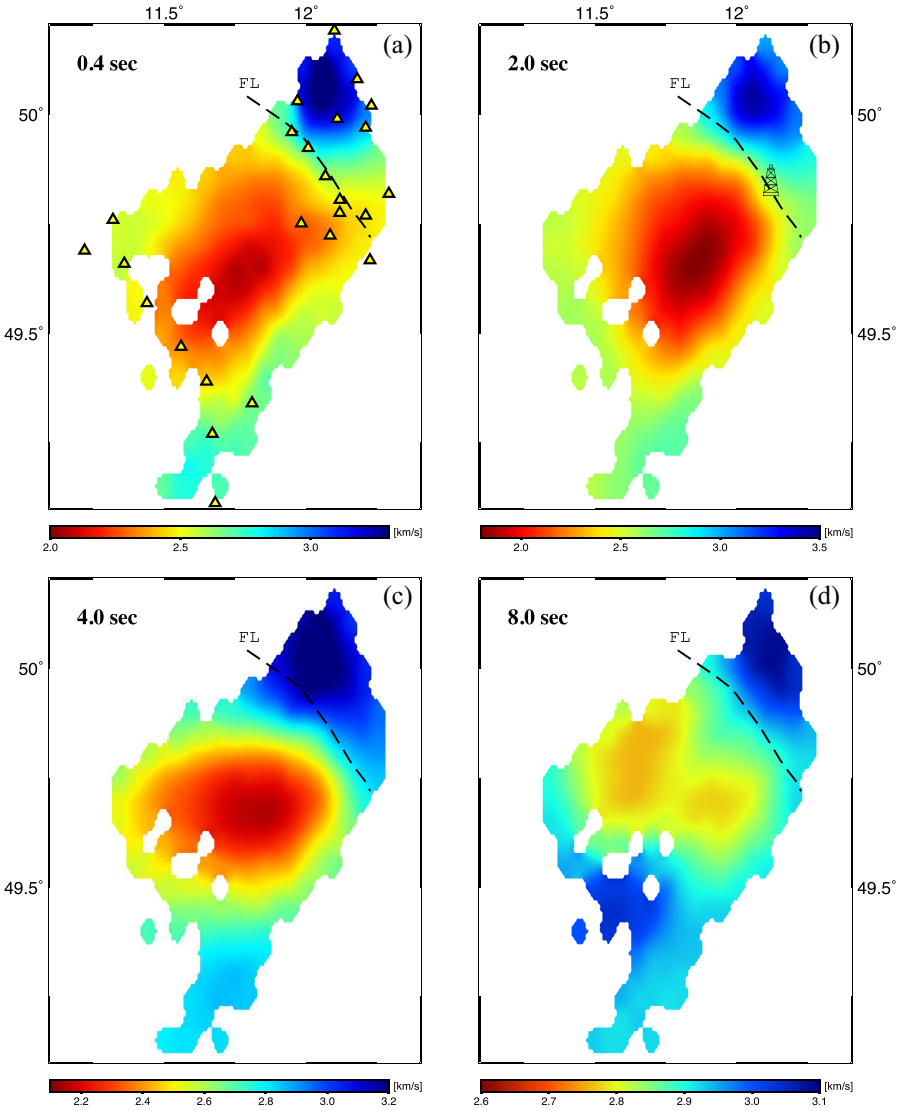

Figure 4. Group-velocity maps at period (a) 0.4 s, (b) 2.0 s, (c) 4.0 s and (d) 8.0 s. Stations used in the inversion are shown by the yellow triangles in (a). Dashed line shows the surface location of the Franconian Line (FL).

range from 2.6 km s^{-1} in the top layer to 3.6 km s^{-1} in the half-space at 15 km depth. We applied no layer weighting, and no fixed velocity in any layer. 30 iterations were done for the inversion, which was sufficient to achieve reasonable fit. The first two iterations were done with higher damping in order to not overshoot the model and the other 28 iterations were done with a lower damping factor. The average-velocity initial model of the inversion is shown in Fig. 6 as well as the distribution of misfit between the theoretical and modelled dispersion curves at all periods. The histogram of the misfit shows small values which are below ±0.1 (Fig. 6a). Fig. 6(b) also shows the histogram of the misfit of the approach 2 (see Section 5.2).

The depth resolution of the inversion is assessed via a normalized resolution matrix of the model. Fig. 6(d) shows the resolution for the average velocity model. It shows a good resolution down to ∼12 km depth, however we present the v_S model down to 10 km depth, where the resolution matrices are quite symmetric. Depth sensitivity kernels are shown in Fig. 7. The kernels are shown for Rayleigh wave fundamental-mode group velocities for a selection of periods between 1 and 10 s. The shear-velocity model obtained via approach 1 is presented in Fig. 8.

5.2 Depth inversion—approach 2

To invert the local group-velocity dispersion curves at each node of the tomography grid, we applied also a second approach, following the procedure described by Kolínský *et al.* (2011, 2014). Inversion is solved by the isometric method. It is a fast algorithm developed by Málek *et al.* (2005) and tested by Málek *et al.* (2007). It combines features of several standard inverse methods, particularly the simplex method, Newton's least squares method and simulated annealing. Typical tasks which are effectively solved by the isometric method are weakly non-linear problems with tens of parameters. The forward problem (dispersion curve computation) is solved by the modified Thomson-Haskell matrix method (Proskuryakova *et al.* 1981). Dispersion curves are computed in a 1-D layered model above a half-space for given values of v_S, v_P and density in the individual layers and in the half-space.

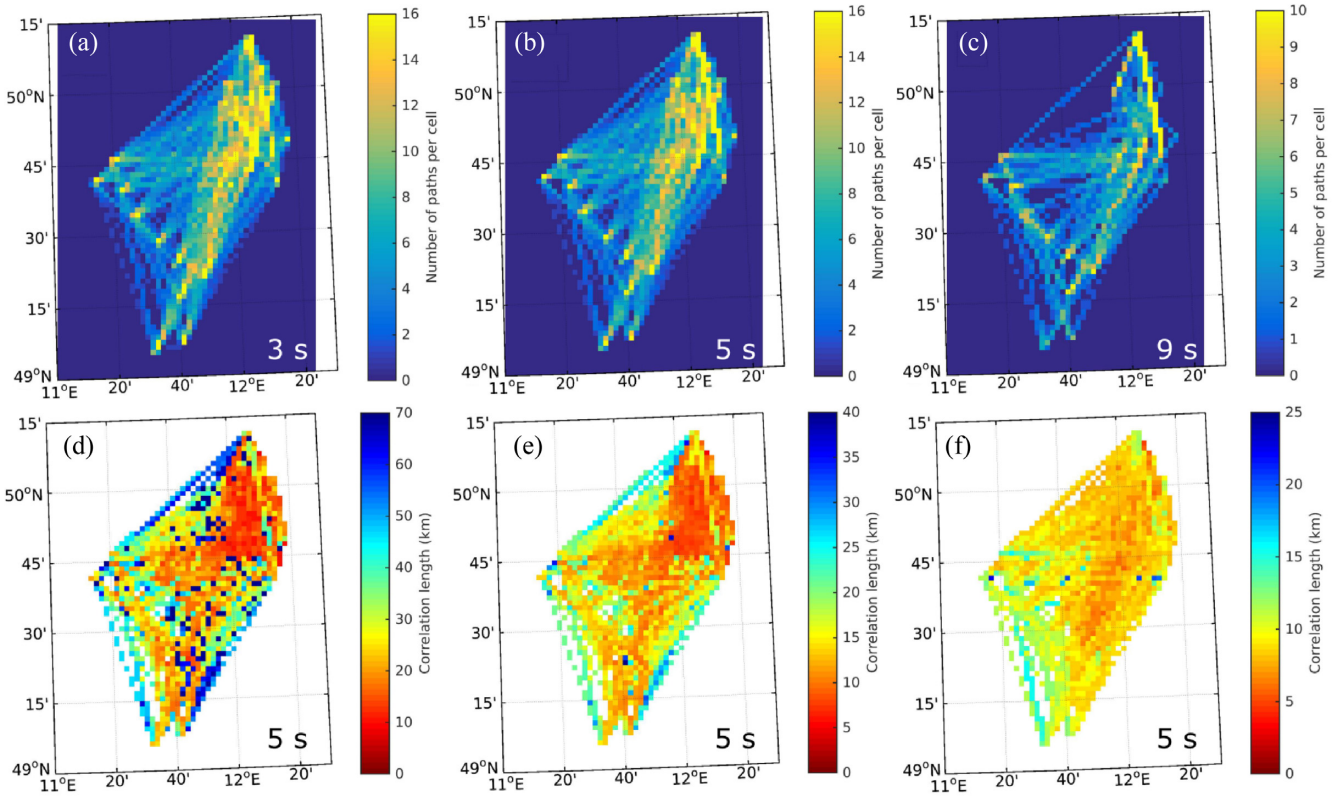

Figure 5. Top panels: path density map for the group-velocity inversion; (a) at 3 s, (b) 5 s and (c) 9 s. The path coverage is generally good for the entire region. Most of the cells have a path density of more than 5 rays per cell. Bottom panels show the resolution of the inversion by correlation length maps for a 5 s centre period. Colours show the correlation length in km, the distance for which the value of the resolution matrix decreases to half. (d) correlation length in the worst direction; (e) mean correlation length for each cell and (f) correlation length in the best direction.

In the inversion, the density was fixed to the ak135 model by Kennett *et al.* (1995) and the v_P/v_S ratio was taken from Bianchi & Bokelmann (2018), who estimated v_S and v_P/v_S for each station. We used an average of the nine v_P/v_S values from Bianchi & Bokelmann (2018) for respective depths in our inversion. Layer thicknesses are chosen manually and are kept unchanged during the inversion. We used 14 layers over the half-space. The thicknesses gradually increase for deeper layers since the resolution ability of the lower frequencies of surface waves is worse. The half-space starts at the depth of 12.6 km. As the density and v_P/v_S ratio are kept unchanged, we effectively inverted only for v_S in every layer as well is in the halfspace. We first inverted the average dispersion curve for the whole region (average of local dispersions at all cells). The result of this inversion was then used as a starting model for the inversion at each cell. The inversion does not depend on the starting model, however, using a model close to the final one saves computational time (Kolínský *et al.* 2011, 2014). The inversion is performed at each cell independently from the others.

The inversion of the dispersion curve is highly non-unique. Different structural models can give similar dispersion curves. To overcome this non-uniqueness of the inversion process, we applied the approach used recently in Belinić *et al.* (2021). The isometric method uses random perturbations of a given model in each iteration to reach a new model, which fits better the measured dispersion curve. Hence, each inversion run can, in general, end up in different local minimum of the misfit function. This we used to sample the space of possible models. Inversion is computed 30 times, and mean velocity distribution with its standard deviation is then determined from all runs. Every run is based on several thousands of iterations. Each single inversion run result is only weakly constrained by the range of velocity differences between neighbouring layers.

The final model calculated as a mean of the 30 individual models differs qualitatively from any of these 30 models. Although its corresponding dispersion curve does not have necessarily the lowest misfit, the mean model usually has the lowest complexity [an average of absolute values of velocity contrasts between the layers, see Kolínský *et al.* (2014)]. The product of misfit and complexity is then much lower for the mean model than the same measure of any of the 30 individual models. It means that the mean model is the closest to the utopia point, where both misfit and complexity are the lowest (see fig. 11 in Kolínský *et al.* 2014). In addition, having the 30 individual models allowed for calculating not only the mean, but also its standard deviation, which is used as a measure of the inversion uncertainties.

Fig. 9 shows examples of inversion for two grid nodes selected in different geological units of the area—see crosses in Fig. 10. Example at node A shows slightly increasing velocities in the upper 2 km and a low-velocity zone between 2 and 6 km depth. Then the velocities increase and the gradient slowly diminishes to almost constant velocities bellow 10 km. Second example shows very high gradient in the uppermost part with a broad low-velocity zone between 1 and 12 km. Generally, velocities are higher in upper parts and lower in deeper parts beneath the node B with respect to node A. Such a characteristics exists for all nodes located respectively in the two geological units. For the node B, the 30 inversion runs are closer to each other than for the node A. However, the misfits evaluating the dispersion curve fit are generally higher in case of node B—see the range between 70.7 and 71.7 $\mathrm{m\,s^{-1}}$ compared to

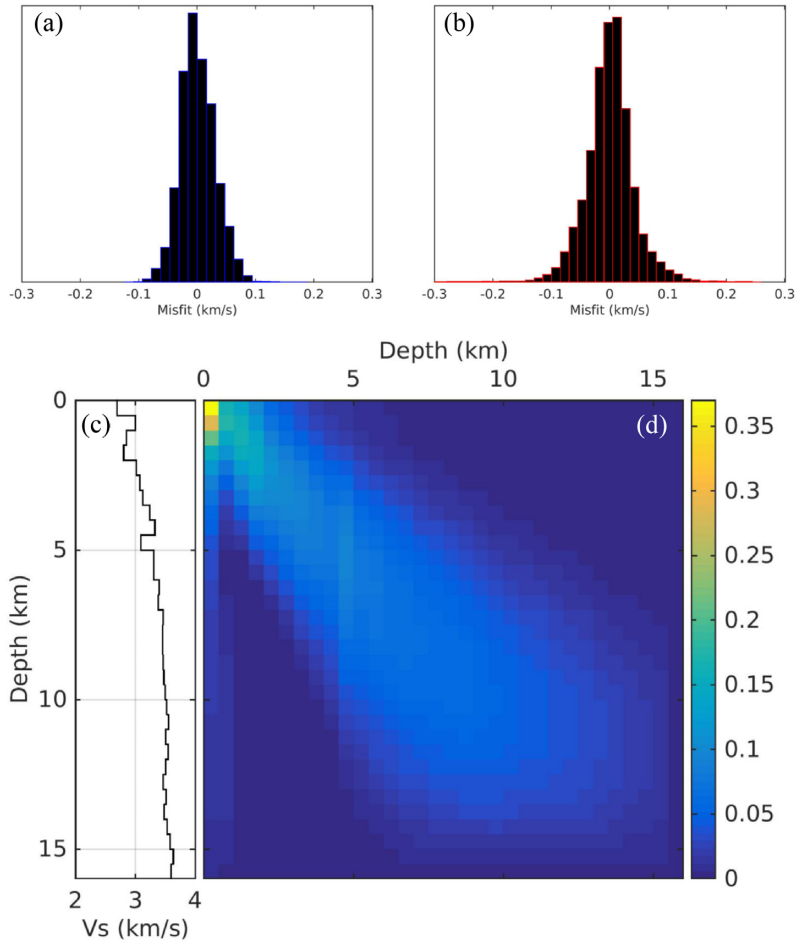

Figure 6. (a) Histograms of the distribution of misfit between synthetic and observed dispersion curves for the approach 1 (see Section 5.1). (b) shows the same for the inversion approach 2 (see Section 5.2) for comparison. (c) The average 1-D velocity model derived for the region that is used as initial model of the inversion approach 1. (d) The resolution matrix elements of the average velocity model from c.

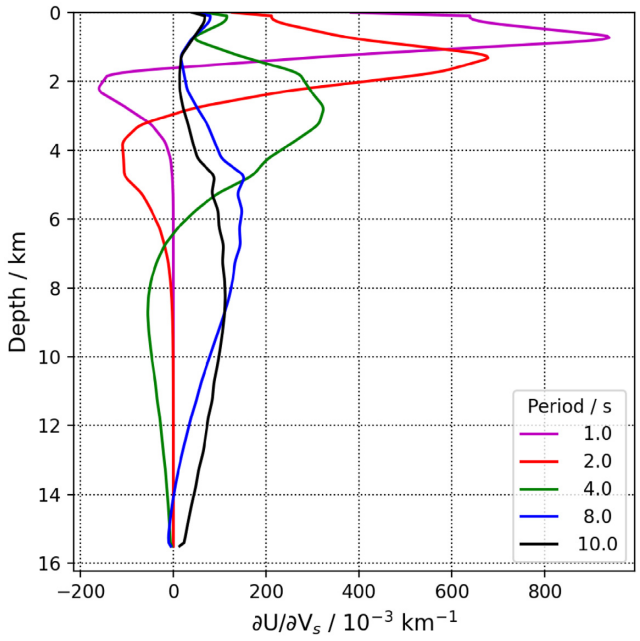

Figure 7. Depth sensitivity kernels for Rayleigh waves group velocity for a selection of periods.

67.5 and 68.5 m s^{-1} in the case of node A. This can be also implied visually from the dispersion curve plots. The complexity of both cases is comparable—see the same range of the vertical axis of the misfit-complexity plots. The red dispersion curve and the red dot correspond to the red mean (final) model. Fig. 6(b) shows histogram of the misfits taken for all periods at all cells. The v_S model derived via the approach 2 is presented in Fig. 10.

6 RESULTS AND DISCUSSION

The velocity models retrieved from the two approaches are rather similar overall, and especially with respect to the location of the fast and slow shear-wave velocities. We are therefore confident in interpreting the high and low velocities displayed in maps as depth slices (Figs 8 and 10) and in cross sections (Fig. 11).

The retrieved shear-velocity maps show two main features in the shallow layers of the crust (from the surface down to about 3 km depth) and two main features in the lower layers of our model (3 to about 9 km depth). We focus our discussion and interpretation on these two depth ranges, and put them into relation with the main geotectonic units (as in Fig. 1) and structural elements known in the study area.

For shallow depths, between 0.2 and about 3 km depth, we notice high velocities (up to 3.6 km s^{-1} close to the surface) confined in the

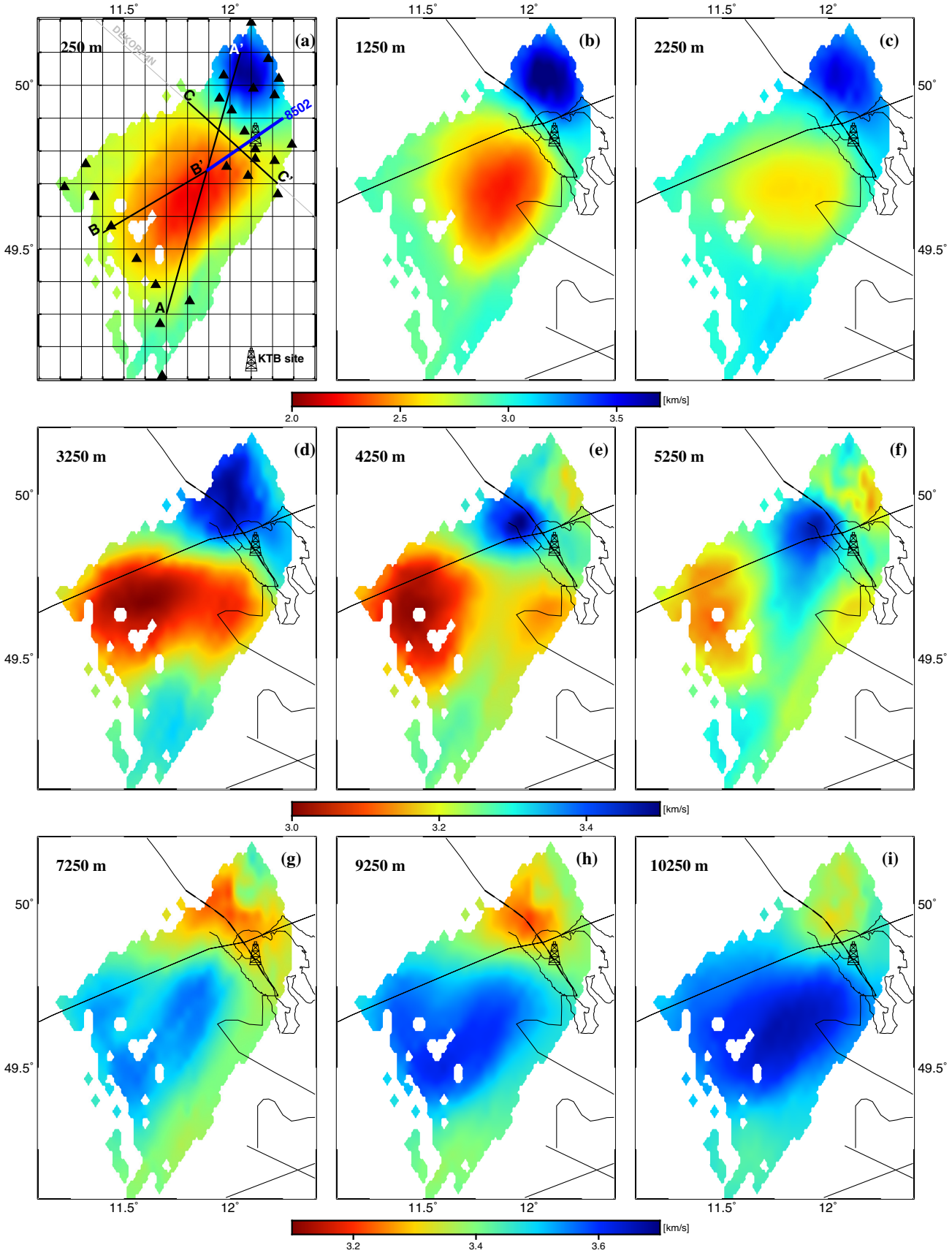

Figure 8. Shear velocity model inverted from the Rayleigh-wave group-velocity maps by approach 1. Thin black lines in maps *b* to *i* show the border of the geotectonic units, as in Fig. 1. Locations of the three profiles of Fig. 11 are presented by the thick lines in *a*. Note the difference in colour scale due to different velocity range at each depth group.

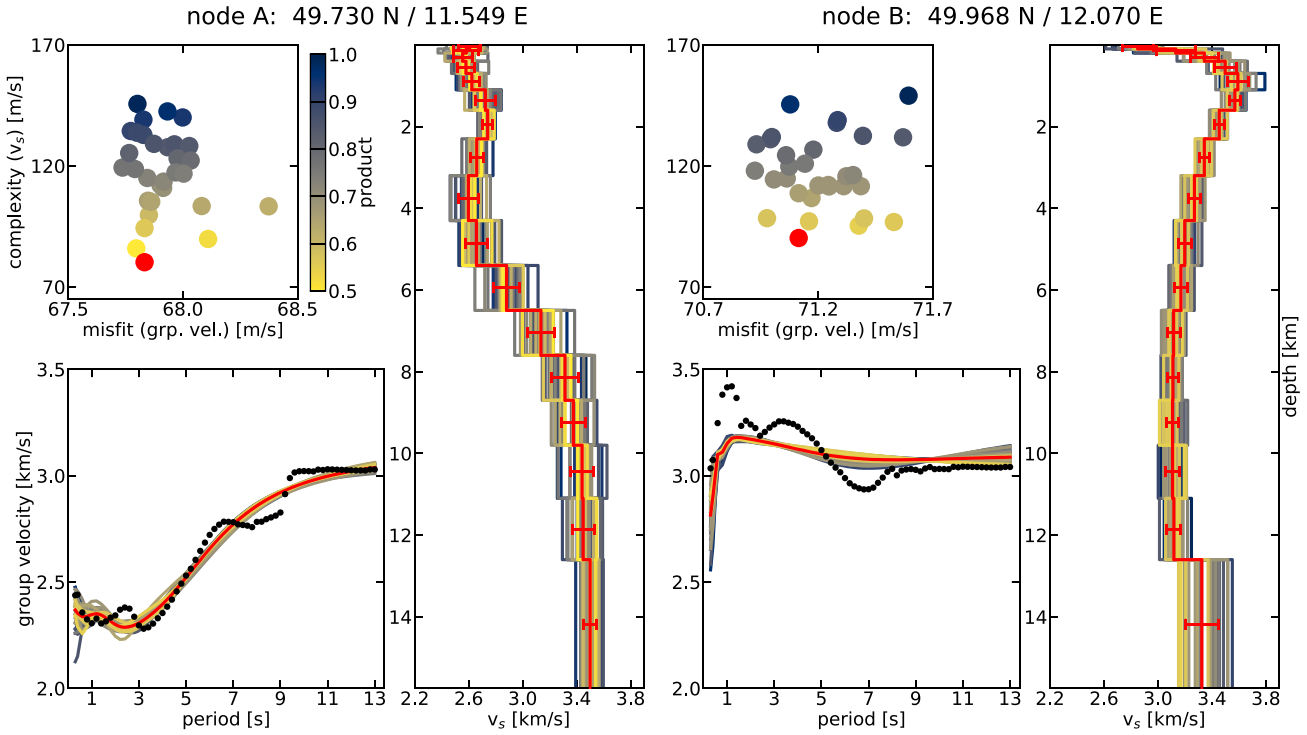

Figure 9. Examples of inversion at two nodes, 'A' and 'B' (see Fig. 10 for location) by approach 2. Local dispersion curve (black dots) is inverted 30 times (u dispersion curves) producing 30 different 1-D models (see the text about how the inversion process uses random perturbations of the models). The mean (red) model is shown with its standard deviation for each layer. Corresponding dispersion curves are shown as well (in red). Dispersion curves are evaluated by misfit and complexity. The dots have colours assigned according to the product of misfit and complexity, which evaluates the whole inversion run with yellow corresponding to lower products, meaning preferred models. The final mean model (red dot) has the lowest complexity and also the lowest misfit-complexity product compared with the 30 individual models.

NE corner of the study area, and low velocities (down to 2 km s^{-1} at the surface) in the SW area. These features are common for both velocity models (Figs 8 and 10). They correspond to well-known features at the surface, (i) the Mesozoic sediments in the SW and (ii) the Falkenberg granites in the NE. The Falkenberg granites are associated with particularly high velocities in the topmost kilometres. Closer to the surface, there is a strong velocity decrease. A rather similar decrease is found in sonic log measurements from the KTB borehole, even though the borehole passes through gneisses and metabasites rather than granites. The decrease in shear velocities is particularly pronounced at depths shallower than 500 m. The decrease agrees with a particularly high porosity at depths shallower than 500 m (Pechnig *et al.* 1997), and it is quite clear that the general velocity decrease toward the surface is due to an increase in porosity.

Higher than average velocities persist until a depth of about 4 km under the outcrop of the Falkenberg granites, which roughly corresponds to the depth range of moderate reflectivity in the KTB8502 profile (see Plate 2 in Harjes *et al.* 1997). Velocities seem to decrease towards the base of the granites. The subsurface under Mesozoic sediments in the SW shows very low shear velocity, especially in a depth range down to about 2 km. This agrees well with the depth range of particularly strong reflectivity (see Plate 2 in Harjes *et al.* 1997), which is consistent with such a layered sequence of strata.

The strong divide between the high-velocity and low-velocity areas also contains the surface trace of the Franconian Lineament (FL). At the surface, it separates basement rocks to the NE from the Mesozoic Basin units to the SW, while at larger depth it runs within the basement, composed of rocks from the ZEV (Zone of Erbendorf-Vohenstrauss). Between 4 and 5 km depth, we observe that the high-velocity patch is shifting towards the SW, and in the deeper slices (about 9 km depth), we notice high velocities to be located to the SW of the FL (while lower velocities are confined to the NE of the same lineament).

To illustrate this switch of velocities around the FL, we inspect cross-sections in Fig. 11. First we compare the KTB8502 active seismic profile (Fig. 11e) published by Emmermann & Lauterjung (1997) to our cross-section also along this profile (Fig. 11c); both of them show the location of the deep drilling site, as reference. The active seismic profile shows the reflectivity of the crust, and it images the trace of the FL that dips to the NE, down to a depth of more than 8 km. Other studies (e.g. Harjes *et al.* 1997) have shown that the FL consists of several faults, and these have been found in the KTB borehole around a depth of 7 km. The reflections appear to be mostly due to fluid-filled fractures and cataclastic fracture zones. A feature as sharp as the FL is not expected to be seen in (ambient noise) surface wave tomography itself, but it is striking that the FL embeds nicely into the lower-scale features seen in (Fig. 11), and it appears that the FL is associated with a NE-dipping low-velocity structure beneath the KTB site. Such a low-velocity structure may well be expected, in the presence of cataclastic rocks and fluids. The thick sedimentary cover is clearly visible in Fig. 11. The low velocities that can be followed to the SW end of the profile BB' (note that the BB' is a prolongation of the KTB8502 profile). In a similar way, the Mesozoic cover is represented in the profiles AA' and CC', perhaps extending somewhat deeper further to the southwest.

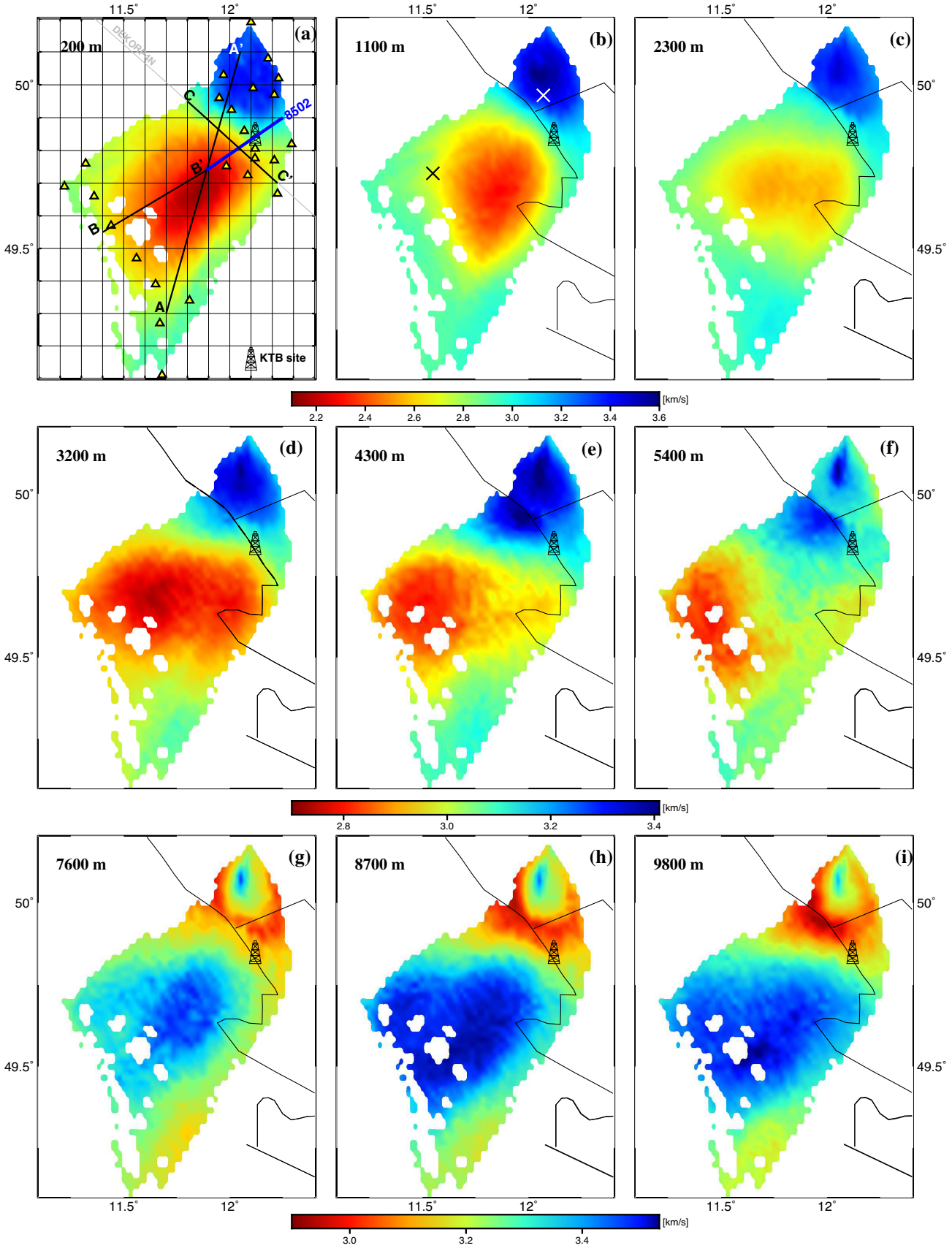

Figure 10. Shear velocity model inverted from the Rayleigh-wave group-velocity maps by approach 2 (as in Fig. 9). Location of the two example nodes, A and B in Fig. 9, are shown by the black and white crosses respectively, in (b). Thin black lines in maps *b* to *i* show the border of the geotectonic units, as in Fig. 1. Note the difference in colour scale due to different velocity range at each depth group.

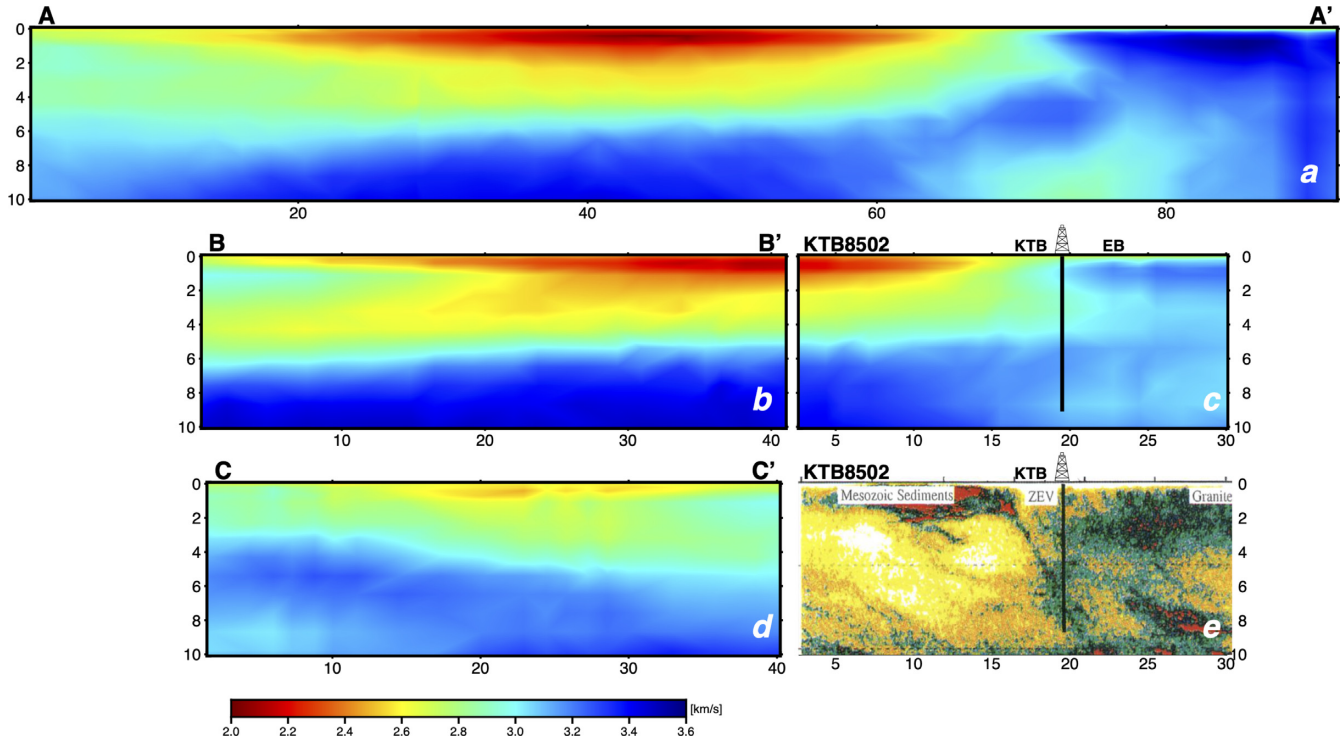

Figure 11. Cross sections of the shear-velocity model presented in this study. (a) Cross-section AA' crossing both the Variscan basement to the NE and the Mesozoic Basin units to the SW of the study area. (b) Cross-section BB' which is an elongation to the seismic reflection profile KTB8502. (c) Cross-section made along the KTB8502 seismic profile. Approximate surface location of the Erbendorf Body (EB) is shown on this profile. (d) CC'cross-section, roughly along the Franconian Lineament. (e) Interpretation of the KTB8502 seismic profile (Emmermann & Lauterjung 1997), shown below *c* for comparison. Profile locations are shown in Figs 8(a) and 10(a).

Before and during the drilling, the so-called Erbendorf body (EB) has received much interest (Emmermann & Lauterjung 1997, and references therein). It has been described as a body that combines high-reflectivity and high v_P, and that probably represents the roots of the ZEV, the extension of which having been previously mapped below the EL. High velocities are retrieved at depths greater than 7 km (see profiles AA' and BB'). These may perhaps be associated with the Erbendorf body (EB). In any case, it is striking that the Erbendorf body is generally presented as 'cut' by the FL, yielding a shallower position to the NE of the FL compared with the SW. Such an asymmetry across the FL (see profile AA') has already been aluded to above. That high-velocity anomaly is extending towards the SE reaching the surface trace of the Erbendorf Line (EL). It may well represent the ZEV and its base zone, the Erbendorf body.

We can thus image the link between the EB and the ZEV, which is seen in profile AA', and can be recognized in the depth slices between 3 and 5 km depth (Figs 8 and 10). Moreover, we can follow the high velocities (possibly related to the EB) both at depth and on map, as drawn by the deep high-velocity body, and which involve an area larger than what was described before (Simon 1993). The general SE-ward dip of the reflective structures in the middle crust [see fig. 2 of O'Brien *et al.* (1997) and fig. 2b of Harjes *et al.* (1997)] may be in line with the general SE-dip of the fast anomaly that is apparent in profile CC'.

Beside isotropic features, also seismic anisotropy has been found in the region, at microscopic scale, and also at seismic scale within the vicinity of the KTB borehole (Rabbel 1994; Rabbel & Mooney 1996; Bianchi & Bokelmann 2019). Inclined azimuthal anisotropy was presented by Bianchi & Bokelmann (2019) at the KW01 station, close to the KTB site, related to the main foliation of the metamorphic rocks of the ZEV, and ascribed to the alignment of the constituting minerals.

Our study considers a wider area, and we present here vertically polarized shear wave velocity (v_{SV}) model derived from Rayleigh-wave group velocities. Fig. S3 shows the v_{SV} of this study together with isotropic shear-wave velocity models from Receiver functions (horizontally polarized, v_{SH}) by Bianchi & Bokelmann (2018) at stations KW01 and KW05. At the KW01, which is located on the ZEV, the v_{SH} is higher than the v_{SV}, which might be due to the presence of radial anisotropy. In Fig. S3, an anisotropic v_{SH} model (Bianchi & Bokelmann 2019) at the KW01 is also plotted. It shows velocities between the v_{SV} and v_{SH}. At the KW05, the v_{SV} (this study) and v_{SH} (from Receiver functions) models are very similar, which may suggest no or weak radial anisotropy. However, in this study, the quality of Love-wave velocity measurements was not good enough to obtain the v_{SH}. Therefore, we were not able to observe Rayleigh–Love wave discrepancy and to separate anisotropic and isotropic effects at the scale of our study area. Another reason for the discrepancy at KW01, at shallow depth, could be lateral smoothing in the ambient noise model, due to the strong velocity anomalies in its vicinity. KW05 is less affected by that, since it is located over smoother structure.

7 CONCLUSIONS

Ambient noise data recorded at 9 temporary and 19 permanent stations around the KTB drilling site were used to perform ambient noise velocity tomography. We have derived a local 3-D v_S model of the upper 10 km of the crust. At shallow depth, we observe a strong

difference in shear wave velocity between the NE and SW ends of the study area. We relate this to the presence of different geotectonic units that are the Falkenberg granites to the NE, the Mesozoic basin to the SW, and the Variscan basement in the centre. We see the depth extension of the granites down to 2–4 km, and of the Mesozoic basin to a similar depth range, with thickness increasing to the west. We identify a decrease in velocity at depth associated to the presence of the Franconian Lineament and the cataclastic zone associated to it. We image the link between the Zone of Erbendorf-Vohenstrauss (ZEV) and its roots (i.e. the Erbendorf Body). The Erbendorf Body probably extends over a larger area than what was described before.

ACKNOWLEDGMENTS

We acknowledge financial support by the Austrian Science Fund (FWF) through project P 26391–AlpArray Austria and P 30707–AlpArray Austria 2. IB acknowledges the support of the Austrian Science Fund (FWF) Project J4314-N29. We thank Galina Simeonova for her help with plotting using Matplotlib (Hunter 2007). The Python Toolbox ObsPy by Beyreuther *et al.* (2010) was used for data handling.

Disclaimer: The views expressed on this paper are those of the authors and do not necessarily reflect the views of the organizations that the authors represent.

DATA AVAILABILITY

Data from the German Regional Seismic Network (BGR) and BayernNetz, Germany (BW) are available through the GFZ webdc data center, http://eida.gfz-potsdam.de/webdc3/. Data from the 9 temporary stations installed from July 2012 to July 2014 are available via request to irene.bianchi@univie.ac.at.

CONFLICT OF INTEREST

The authors declare that they have no conflict of interest.

REFERENCES

Barmin, M.P., Ritzwoller, M.H. & Levshin, A.L., 2001. A fast and reliable method for surface wave tomography, *Pure appl. Geophys.,* **158**(8), 1351–1375.

Belinić, T., Kolínský, P. & Stipčević, J., 2021. Shear-wave velocity structure beneath the Dinarides from the inversion of Rayleigh-wave dispersion, *Earth planet. Sci. Lett.,* **555,** doi:10.1016/j.epsl.2020.116686.

Berckhemer, H. *et al.*, 1997. Petrophysical properties of the 9-km-deep crustal section at ktb, *J. geophys. Res.,* **102**(B8), 18 337–18 361.

Beyreuther, M., Barsch, R., Krischer, L., Megies, T., Behr, Y. & Wassermann, J., 2010. ObsPy: a Python toolbox for seismology, *Seismol. Res. Lett.,* **81**(3), 530–533.

BGR, 1976. German Regional Seismic Network (GRSN), Federal Institute for Geosciences and Natural Resources.

Bianchi, I. & Bokelmann, G., 2018. Imaging the Variscan suture at the KTB deep drilling site, Germany, *Geophys. J. Int.,* **213**(3), 2138–2146.

Bianchi, I. & Bokelmann, G., 2019. Probing crustal anisotropy by receiver functions at the deep continentaldrilling site KTB in Southern Germany, *Geophys. Prospect.,* **67,** 2450–2464.

Bianchi, I., Anselmi, M., Apoloner, M.T., Qorbani, E., Gribovski, K. & Bokelmann, G., 2015. The installation campaign of 9 seismic stations around the ktb site to test anisotropy detection by the receiver function technique, *Adv. Geosci.,* **41,** 11–23.

Burrett, C.F., 1972. Plate tecotnics and the Hercynian Orogeny, *Nature,* **239,** 155–157.

BW, 2001. Department of Earth And Environmental Sciences, Geophysical Observatory, University of München.

Campillo, M. & Roux, P., 2015. 1.12: Crust and lithospheric structure - seismic imaging and monitoring with ambient noise correlations, in *Treatise on Geophysics,* 2nd end, pp. 391–417, ed. Schubert, G., Elsevier.

DEKORP research group, 1988. Results of the DEKORP 4/KTB Oberpfalz deep seismic reflection investigations, *J. Geophys.,* **62,** 69–101.

Dürbaum, H., Reichert, C. & Bram, K., 1990. Integrated Seismics Oberpfalz 1989. Long-term Logging and Testing Programme of the KTB-Oberpfalz VB, KTB Report (DEKORP Report), 208pp.

Dürbaum, H.-J., Reichert, C., Sadowiak, P. & Bram, K., 1992. Integrated seismics oberpfalz 1989. data evaluation and interpretation as of October 1992, KTB Report (DEKORP Report), 373pp.

Emmermann, R. & Lauterjung, J., 1997. The German continental deep drilling program KTB: overview and major results, *J. geophys. Res.,* **102**(B8), 18 179–18 201.

Emmermann, R. & Wohlenberg, J., 1989. *The German Continental Deep Drilling Program (KTB),* Springer-Verlag.

Enderle, U., Schuster, K., Prodehl, C., Schulze, A. & Bribach, J., 1998. The refraction seismic experiment GRANU95 in the Saxothuringian belt, southeastern Germany, *Geophys. J. Int.,* **133**(2), 245–259.

Franke, W., 1989. Variscan plate tectonics in Central Europe - current ideas and open questions, *Tectonophysics,* **169,** 221–228.

Hansen, P.C. & O'Leary, D.P., 1993. The use of the L-curve in the regularization of discrete ill-posed problems, *SIAM J. Sci. Comput.,* **14**(6), 1487–1503.

Harjes, H.-P. & Seidl, D., 1977. Digital recording and analysis of broadband seismic data at the Graefenberg (GRF) array, *J. Geophys.,* **44**(1), 511–523.

Harjes, H.-P. *et al.*, 1997. Origin and nature of crystal reflections: results from integrated seismic measurements at the KTB superdeep drilling site, *J. geophys. Res.,* **102,** 18 267–18 288.

Herrmann, R.B., 2013. Computer programs in seismology: an evolving tool for instruction and research, *Seismol. Res. Lett.,* **84**(6), 1081–1088.

Hirschmann, G., 1996. KTB—the structure of a Variscan terrane boundary: seismic investigation—drilling—models, *Tectonophysics,* **264**(1), 327–339.

Holzförster, F., Peterek, A. & Rabold, J.M., 2011. KTB deep drilling site and Czech-Bavarian Geopark—two best practice examples of geoscience outreach, in *Geological Field Trips in Central Western Europe,* Geological Society of America.

Hunter, J.D., 2007. Matplotlib: a 2D graphics environment, *Comp. Sci. Eng.,* **9**(3), 90–95.

Kennett, B.L., Engdahl, E. & Buland, R., 1995. Constraints on seismic velocities in the Earth from traveltimes, *Geophys. J. Int.,* **122**(1), 108–124.

Kolínský, P. & Brokešová, J., 2007. The Western Bohemia uppermost crust shear wave velocities from Love wave dispersion, *J. Seismol.,* **11,** 101–120.

Kolínský, P., Málek, J. & Brokešová, J., 2011. Shear wave crustal velocity model of the Western Bohemian Massif from Love wave phase velocity dispersion, *J. Seismol.,* **15,** 81–104.

Kolínský, P., Valenta, J. & Málek, J., 2014. Velocity model of the Hronov-Poříčí Fault Zone from Rayleigh wave dispersion, *J. Seismol.,* **18,** 617–635.

Lévêque, J.-J., Rivera, L. & Wittlinger, G., 1993. On the use of the checkerboard test to assess the resolution of tomographic inversions, *Geophys. J. Int.,* **115**(1), 313–318.

Lukešová, R., Fojtíková, L., Málek, J. & Kolínský, P., 2019. Seismic waves velocities inferred from the surface waves dispersion in the Malé Karpaty Mountains, Slovakia, *Acta Geodyn. Geomater.,* **16**(4(196), 451–464.

Málek, J., Horálek, J. & Janský, J., 2005. One-dimensional qP-wave velocity model of the upper crust for the West Bohemia/Vogtland earthquake swarm region, *Stud. Geophys. Geod.,* **49,** 501–524.

Málek, J., Růžek, B. & Kolář, P., 2007. Isometric method: efficient tool for solving non-linear inverse problems, *Stud. Geophys. Geod.,* **51,** 469–490.

Meissner, R. & Bortfeld, R., 1990. *Dekorp-Atlas,* pp. 19, Springer, 80 sections.

O'Brien, P., Duyster, J., Grauert, B., Schreyer, W., Stöckhert, B. & Weber, K., 1997. Crustal evolution of the KTB drill site: From oldest relics to the Late Hercynian granites, *J. geophys. Res.,* **102,** 18 203–18 220.

Pechnig, R., Haverkamp, S., Wohlenberg, J., Zimmermann, G. & Burkhardt, H., 1997. Integrated log interpretation in the german continental deep drilling project, *J. geophys. Res.,* **102,** 18 363–18 390.

Poli, P., Pedersen, H.A. & Campillo, M., 2013. Noise directivity and group velocity tomography in a region with small velocity contrasts: the northern Baltic shield, *Geophys. J. Int.,* **192**(1), 413–424.

Proskuryakova, T., Novotný, O. & Voronina, E., 1981. *Studies of the Earth's Structure by the Surface-Wave Method (Central Europe) (Izuchenie stroeniya Zemli metodom poverkhnostnykh voln (Tsentral'naya Evropa)),* pp. 92, Nauka, Moscow, in Russian.

Qorbani, E., Zigone, D., Handy, M.R., Bokelmann, G. & Group, A.-E.W., 2020. Crustal structures beneath the Eastern and Southern Alps from ambient noise tomography, *Solid Earth,* **11**(5), 1947–1968.

Rabbel, W., 1994. Superdeep vertical seismic profiling at the KTB deep drill hole (Germany): Seismic close-up view of a major thrust zone down to 8.5 km depth, *Tectonophysics,* **232,** 329–341.

Rabbel, W. & Mooney, W., 1996. Seismic anisotropy of the crystalline crust: what does it tell us? *Terra Nova,* **8,** 16–21.

Schippkus, S., Zigone, D., Bokelmann, G., Group, A.W. & Lab, E.-S.E., 2019. Azimuthal anisotropy in the wider Vienna basin region: a proxy for the present-day stress field and deformation, *Geophys. J. Int.,* **220**(3), 2056–2067.

Schweitzer, J., Fyen, J., Mykkeltveit, S., Gibbons, S.J., Pirli, M., Kühn, D. & Kværna, T., 2012. Seismic arrays, in *New Manual of Seismological Observatory Practice (NMSOP-2),* pp. 1–80, Deutsches GeoForschungsZentrum GFZ.

Shapiro, N.M. & Campillo, M., 2004. Emergence of broadband Rayleigh waves from correlations of the ambient seismic noise, *Geophys. Res. Lett.,* **31**(7), doi:10.1029/2004GL019491.

Shapiro, N.M., Campillo, M., Stehly, L. & Ritzwoller, M.H., 2005. High-resolution surface-wave tomography from ambient seismic noise, *Science,* **307**(5715), 1615–1618.

Simon, M., 1993. Entwicklung eines 3D-Migrationsverfahrens mit Anwendung auf seismische Daten aus dem Umfeld der Kontinentalen Tiefbohrung Oberpfalz, *PhD thesis*, pp. 186, Ludwig-Maximilians-Universität, München.

Stehly, L., Fry, B., Campillo, M., Shapiro, N.M., Guilbert, J., Boschi, L. & Giardini, D., 2009. Tomography of the Alpine region from observations of seismic ambient noise, *Geophys. J. Int.,* **178**(1), 338–350.

Stettner, G., 1992. *Geologie im Umfeld der Kontinentalen Tiefbohrung, Oberpfalz,* pp. 240, Bayerisches Geologisches Landesamt.

Toksöz, M.N. & Lacoss, R.T., 1968. Microseisms: mode structure and sources, *Science,* **3817**(159), 872–873.

Zigone, D., Ben-Zion, Y., Campillo, M. & Roux, P., 2015. Seismic tomography of the southern California plate boundary region from noise-based Rayleigh and Love waves, *Pure appl. Geophys.,* **172**(5), 1007–1032.

Zigone, D., Ben-Zion, Y., Lehujeur, M., Campillo, M., Hillers, G. & Vernon, F.L., 2019. Imaging subsurface structures in the San Jacinto fault zone with high-frequency noise recorded by dense linear arrays, *Geophys. J. Int.,* **217**(2), 879–893.

SUPPORTING INFORMATION

Supplementary data are available at *GJI* online.

Figure S1. Correlation tensor including nine intercomponents RR, RT, RZ, TR, TT, TZ, ZR, ZT and ZZ. The figure shows propagation of surface waves through all station pairs. Rayleigh waves appear on the RR, RZ, ZR, ZZ and Love waves on the TT. Note the slightly faster arrival of the Love waves with respect to the Rayleigh wave. The cross-correlations are stacked in 2 km distance bins and sorted according to station distance.

Figure S2. Plot of all group velocities extracted for the study area. Each line shows Rayleigh-wave group velocity for one node. Black thick line shows the averaged dispersion curve over all nodes.

Figure S3. Figure comparing the shear wave velocity depth profile from this study (red line) and from Receiver Functions (blue line) (Bianchi & Brockelman 2018) at stations KW01 and KW05. KW01 is located close to the KTB drilling site. Anisotropic *S*-wave velocity–depth profile (Bianchi & Brockelman 2019) is also presented (green line) for KW01. Dashed lines represent the amount of anisotropy in each layer.

Please note: Oxford University Press is not responsible for the content or functionality of any supporting materials supplied by the authors. Any queries (other than missing material) should be directed to the corresponding author for the paper.